

# Two-year observations of the Jupiter polar regions by JIRAM on board Juno

A. Adriani<sup>1</sup>, A. Bracco<sup>2</sup>, D. Grassi<sup>1</sup>, M.L. Moriconi<sup>3</sup>, A. Mura<sup>1</sup>, G. Orton<sup>4</sup>, F. Altieri<sup>1</sup>, A. Ingersoll<sup>5</sup>, S.K. Atreya<sup>6</sup>, J.I. Lunine<sup>7</sup>, A. Migliorini<sup>1</sup>, R. Noschese<sup>1</sup>, A. Cicchetti<sup>1</sup>, R. Sordini<sup>1</sup>, F. Tosi<sup>1</sup>, G. Sindoni<sup>8</sup>, C. Plainaki<sup>8</sup>, B.M. Dinelli<sup>3</sup>, D. Turrini<sup>1</sup>, G. Filacchione<sup>1</sup>, G. Piccioni<sup>1</sup>, and S.J. Bolton<sup>9</sup>.

<sup>1</sup>INAF - Istituto di Astrofisica e Planetologia Spaziali, Roma, Italy

<sup>2</sup>Georgia Institute of Technology, Atlanta, Georgia, USA

<sup>3</sup>CNR - Istituto di Scienze dell'Atmosfera e del Clima, Bologna and Roma, Italy

<sup>4</sup>Jet Propulsion Laboratory, California Institute of Technology, Pasadena, California, USA

<sup>5</sup>California Institute of Technology, Pasadena, California, USA

<sup>6</sup>University of Michigan, Ann Arbor, Michigan, USA

<sup>7</sup>Cornell University, Ithaca, New York, USA

<sup>8</sup>Agenzia Spaziale Italiana, Roma, Italy

<sup>9</sup>Southwest Research Institute, San Antonio, Texas, USA

Corresponding author: Alberto Adriani ([alberto.adriani@inaf.it](mailto:alberto.adriani@inaf.it))

## Key Points:

- The Jupiter's polar cyclonic structures did not change much in two years of observations from February 2017 to February 2019.
- Abundances of some atmospheric minor constituents measured in the hottest spots of the polar regions, higher values registered in the south.
- Earth oceanic cyclones analogies suggest a well-mixed upper boundary layer on Jupiter's Poles.

## Abstract

We observed the evolution of Jupiter's polar cyclonic structures over two years between February 2017 and February 2019, using polar observations by the Jovian InfraRed Auroral Mapper, JIRAM, on the Juno mission. Images and spectra were collected by the instrument in the 5- $\mu\text{m}$  wavelength range. The images were used to monitor the development of the cyclonic and anticyclonic structures at latitudes higher than  $80^\circ$  both in the northern and the southern hemispheres. Spectroscopic measurements were then used to monitor the abundances of the minor atmospheric constituents water vapor, ammonia, phosphine and germane in the polar regions, where the atmospheric optical depth is less than 1. Finally, we performed a comparative analysis with oceanic cyclones on Earth in an attempt to explain the spectral characteristics of the cyclonic structures we observe in Jupiter's polar atmosphere.

## Plain Language Summary

The Jovian InfraRed Auroral Mapper (JIRAM) is an instrument on-board the Juno NASA spacecraft. It consists of an infrared camera, for mapping both Jupiter's auroras and atmosphere, and a spectrometer. In February 2017, the complex, cyclonic structures that characterize the Jupiter's polar atmospheres were discovered. Here, we report the evolution of those cyclonic structures during the 2 years following the discovery. We use for this purpose infrared maps built by the JIRAM camera images collected at wavelengths around 5  $\mu\text{m}$ .

50 The cyclones have thick clouds which obstruct most of the view of the deeper atmosphere. However,  
51 some areas, near the cyclones, are only covered by thin clouds allowing the spectrometer to see deeper  
52 in the atmosphere. In those areas, the instrument was able to detect spectral signatures that permitted  
53 estimation of abundances of water vapor, ammonia, phosphine and germane. Those gases are minor  
54 but significant constituents of the atmosphere.

55 Finally, the dynamics of the Jupiter's polar atmosphere are not well understood and are still under  
56 study. Here, to suggest possible mechanisms that governs the polar dynamics, we attempted a  
57 comparative analysis with some Earth oceanic cyclones that show similarities with the Jupiter ones.  
58

59  
60 **Keywords:** Jupiter, Planetary Atmosphere, Polar Regions, Composition, Mesoscale Dynamics  
61

## 62 1. Introduction

63  
64 The Juno mission entered into Jupiter orbit in July, 2016 [Bolton et al. 2017]. The Jovian InfraRed  
65 Auroral Mapper, JIRAM, is part of the payload of the spacecraft [Adriani et al. 2017]. Key goals of  
66 this instrument are to collect both  $\sim 5\text{-}\mu\text{m}$  imaging (M band filter: 4.5 to 5  $\mu\text{m}$ ) and spectral  
67 observations in the 2-5  $\mu\text{m}$  range with a spectral resolution of about 15 nm to study Jupiter's  
68 atmosphere. The methane transparency window, around 5,  $\mu\text{m}$  is a spectral region dominated by the  
69 atmospheric thermal emission. However, the thermal emission is modulated by the presence of the  
70 clouds and, thus, the depth of the infrared sounding depends on the cloud thickness. In the absence  
71 of clouds and for small optical thickness the infrared sounding at wavelengths around 5  $\mu\text{m}$  can reach  
72 depths of 4-5 bar. The imager focal plane is divided in two areas by the presence of two optical filters:  
73 one in band L dedicated to auroral mapping and the other in band M for atmospheric observations.  
74 The auroral signal is weaker than the atmospheric thermal emission, and thus the imager has to use  
75 different integration times in according with the target of interest. This fact implies that the  
76 observations targeting the aurorae or the atmospheric thermal emissions cannot be operated  
77 simultaneously. The imager and the spectrometer have a spatial resolution of 250  $\mu\text{rad}$  and are  
78 operated simultaneously.

79 The great advantage of Juno's instruments, compared to all the others that have observed Jupiter for  
80 years from Earth and from other space missions, is that Juno is in a polar orbit, allowing an  
81 unprecedented view of the planet's poles.

82 On February 2<sup>nd</sup> 2017, during the fourth fly-by, JIRAM had the opportunity to observe the polar  
83 atmosphere of Jupiter for the first time [Adriani et al. 2018]. Those observations, together with those  
84 of the visible JunoCam imager [Hansen et al, 2014], allowed us to survey for the first time the  
85 dynamical structure of the polar atmosphere of the planet. The North Pole exhibits a polar cyclone  
86 (or NPC) surrounded by eight circumpolar cyclones (or CPCs) while the South Pole is characterized  
87 by five cyclones surrounding a polar cyclone. The CPCs have approximately the same size as their  
88 respective central polar cyclones; the southern cyclones are larger than the northern ones.

89 JIRAM's observation of Jupiter's poles has continued since February 2017 during fly-bys with  
90 favorable spacecraft attitudes and when auroral observations by JIRAM were not scheduled. For the  
91 sake of simplicity we identify **Juno** orbits with the label PJ (PeriJove) followed by the orbit number.  
92 The spacecraft attitude was generally not favorable to the JIRAM observations during orbits when  
93 the mission optimized the gravitational mapping of Jupiter (GRAV orbits). Additionally, the  
94 instrument can only observe targets that are within  $\pm 3^\circ$  of the plane orthogonal to the spacecraft spin  
95 axis. A limited number of orbits have been dedicated to remote sensing instrumentation on board of  
96 Juno. During orbits when the MicroWave Radiometer (MWR) was the prime instrument, JIRAM  
97 could observe the planet during the approach and reasonably cover the North Pole. Orbit 9 (PJ9) was  
98 the last one in which JIRAM had a reasonably good coverage of the Pole. On the other hand, the

99 South Pole could be observed almost during every perijove pass with good coverage and spatial  
100 resolution.

101 Table 1 provides a summary of the observations for which we were able to obtain good coverage of  
102 the polar regions: four for the North Pole and ten for the South Pole. Observations with more limited  
103 coverage have been excluded from this analysis. Given that Juno maintains a polar orbit of about 53  
104 days, that is the minimum time interval between two successive observations reported here. The  
105 spatial resolution at the 1-bar pressure level is variable and ranges from about 15 km to about 60 km,  
106 depending on the position of the spacecraft in the orbit.

107 In this paper we report and discuss the observations made by the JIRAM imager in band M of the  
108 CPC. Moreover, while tropospheric composition in hot spots and in extended regions at Jupiter's low  
109 and intermediate latitudes has been investigated by a number of authors on the basis of spacecraft and  
110 ground-based telescope data [e.g. Giles et al. 2015 and Giles et al. 2017], no study has yet covered  
111 the polar regions. However, starting from the Juno's fourth perijove (PJ4, February 2nd 2017) JIRAM  
112 has gradually acquired extensive observations over both poles. Here we calculate the tropospheric  
113 content of water, ammonia, phosphine and germane at Jupiter's polar regions from JIRAM spectral  
114 data in those areas where the atmospheric optical depth is less than 1.

115 Finally, in order to contribute to understanding of the dynamic processes that regulate the circumpolar  
116 structure of Jupiter we make comparisons with oceanic cyclones observed on Earth.

117

## 118 2. Observations

119 Subsequent images acquired by JIRAM are composed in a single picture, called mosaic. Table 1  
120 reports the pixel resolutions of the mosaics built by single stereographic maps based on System III  
121 longitude and planetocentric latitude coordinates and the number of images used for the relative  
122 mosaics. Mosaics are shown in Figures 1, 2 and 3: Figures 1 refers to the North Pole observations  
123 while Figures 2 and 3 refer to those at the South Pole. All the observations and the analysis reported  
124 here are at a latitude higher than 80°N and 80°S. All the single images used in this work, as well as  
125 the plots in the mosaics of Figures 1, 2 and 3, have been corrected by Beer's law, and the data were  
126 chosen so that the emission angle (the angle between the normal to the planet at the pixel location  
127 and the direction of the spacecraft) was always lower than 60° (except for the Northern cyclones #5  
128 and #6 during PJ9). Figures 1, 2 and 3 are plotted in term of optical depth,  $\tau = \log(I_0/I)$ , that is  
129 normalized to the value  $I_0 = 0.65624 \text{ Wm}^{-2}$  which is the maximum radiance measured at latitudes  
130 higher than 80° in both the north or in the south. In this scheme, light colors represent thicker clouds.  
131 That is, the figures show the cloudiness in the polar regions making them easier to compare to the  
132 visual camera observations of JunoCam, the camera onboard Juno. All JunoCam images since the  
133 beginning of the mission are available on the Juno Mission website at  
134 <https://www.missionjuno.swri.edu/junocam>.

135 All the reported data have a geographical reference. We use NAIF-SPICE [Acton, 1996] and ENVI  
136 tools (by <https://www.harrisgeospatial.com/Software-Technology/>) for every geometric calibration  
137 and processing of images. Ultimately, the images in Figures 1, 2 and 3 are composites obtained by  
138 assembling different image sequences taken by JIRAM. They are plotted in geographic coordinates  
139 and show the maps of  $\tau$  (as defined above) for the two poles. Significant differences between North  
140 and South are readily apparent from a visual comparison of Figure 1 versus Figures 2 and 3.

141 In Figure 1, we present the sequence of four North Pole observations summarized in Table 1. As  
142 stated previously by Adriani et al. [2018], the dynamic structure of this pole is shaped in such a way

143 that the cyclones surrounding the polar one are approximately located on the vertices of a ditetragonal  
144 pattern. Some of the cyclones kept their cloud patchy structures in the eight months between PJ4 and  
145 PJ9, while others showed more clearly ordered cloudy spiral configurations with small cyclones or  
146 anticyclones inside the main structure. In general, the CPCs arrangement was quite stable during this  
147 entire period, and the internal structure of the single cyclones did not change significantly– including  
148 the one visible in PJ10.

149 Beside the small fluctuation of the CPCs around their average position, a big anticyclone was located  
150 around 87°N latitude. It has been present since the first JIRAM observation during PJ4 (February  
151 2017) and was still present during PJ10, a period slightly longer than 10 months. In this time span, it  
152 grew slightly in size from about 1,400 km up to about 2,000 km in diameter, oscillating between 80°E  
153 and 120°E longitudes in the “channel” between the polar cyclone and the circumpolar cyclones. Its  
154 changes in position can be clearly detected in Figure 1. Unfortunately, its later evolution could not be  
155 monitored due to the poor JIRAM coverage of the North Pole that resulted from the spacecraft attitude  
156 change during the remaining part of the mission.

157 In Figures 2 and 3 we present the sequence of ten South Pole observations summarized in Table 1.  
158 As already stated by Adriani et al. [2018] following the PJ4 observation in February 2017, the South  
159 Pole configuration is quite different from the northern one. The South Pole observations have  
160 continued on regular basis, and here we report about the evolution between PJ4 and PJ18. During a  
161 time lapse of two years the pentagonal structure remained substantially unchanged, with only  
162 occasional perturbations.

163 As in the north, the six cyclones slightly changed their internal structure. In particular, as can be seen  
164 in Figures 2 and 3, the group formed by cyclones 3, 4 and 5 were more stable over the two-year period  
165 while the cyclones 1, 2 and 6 were more variable in terms of cloudiness. Unlike the North Pole,  
166 however, no long-lasting anticyclonic structures nested within the pentagonal structure were observed  
167 at the South Pole. During the first year, anticyclones appeared episodically within the cyclonic  
168 assembly but never lasted to the following perijove. On the other hand, a few relatively large  
169 anticyclones were present in the second year of the mission, from PJ13 onward. Moreover, toward  
170 the end of the period a new feature appeared between the CPCs #5 and #6 (see Figure 4 for the  
171 identification of CPC numbers). This structure is reminiscent of a vortex dipole whose embryo was  
172 already recognizable during PJ15. During PJ18 the Southern CPCs appeared to move to a hexagonal  
173 shape where the new-born vortex is joining the previous ones around the central cyclone.

174 Figure 4 illustrates the position of the cyclones and the anticyclones with diameters larger than 1000  
175 km observed in the polar region of both hemispheres. In the almost 9 months during which we could  
176 get good coverage of the North Pole no anticyclones of sizes larger than 1000 km were observed at  
177 latitudes higher than 80°N beside the one hovering at 87°N between the NPC and the CPCs. On the  
178 other hand, a large number of anticyclones were observed in the southern regions, particularly at  
179 longitudes between 100°E and 300°E. Most of them appeared to be connected to a cyclone in a dipole  
180 configuration. Sometimes the cyclone was one of the CPCs, as in the case of CPC#5 where the  
181 anticyclone was still present during PJ19 (not shown here). During PJ18, CPC#6 moved significantly  
182 towards lower longitudes leaving space for the intrusion of a cyclone/anticyclone dipole that could  
183 anticipate the formation of a new CPC. Other cyclones with diameters larger than 1000 km  
184 occasionally grew outside the CPCs ring, but they never appeared to last for more than a 53-day  
185 perijove pass.

186 The average radiances measured in the spectral range 4.5-5.0  $\mu\text{m}$  are systematically higher in the  
187 north than in the south. In the north the average value is 0.133  $\text{Wm}^{-2}$ , while in the south the average  
188 is 0.069  $\text{Wm}^{-2}$  [Figure 5 panel (a)]. During PJ4 the southern radiance was at its highest value of 0.1  
189  $\text{Wm}^{-2}$  followed by an abrupt decay of about 50% during PJ6, after 106 days.

190 A slow but progressive increase has been observed after PJ6 [see Figure 4 panel (a) for details]. Panel  
191 (a) of Figure 5 shows also the statistics of the pixels' brightness of the two poles in terms of radiance.  
192 In the legend, the corresponding average brightness temperature for each PJ and at latitudes higher  
193 than  $80^\circ$  N/S is also given. A direct comparison between North and South can be only done for the  
194 first year, as no north pole images in the infrared range are available after December 2017.

195 Some single cyclone characteristics have been investigated in order to monitor the changes that  
196 occurred in the two years of observations, from February 2017 to February 2019. Figure 5 also  
197 accounts for changes in the average diameters [panel (b)] and cloudiness [ $\tau$ , in panel (c)] of the single  
198 cyclones versus time from PJ4 to PJ18. The diameters of the northern and southern cyclones are  
199 substantially different. The average diameter of the northern cyclones is about 4,600 km. Southern  
200 cyclones, being fewer than but occupying approximately the same latitudinal extension as the  
201 northern ones, are systematically larger, their average diameter reaches approximately 6,300 km.  
202 Another difference between south and north is the relative size of the polar cyclone with respect the  
203 surrounding CPCs. While the size of the southern polar cyclone (SPC) is commensurate with the  
204 surrounding CPCs, the northern one (NPC) is significantly larger than its surrounding CPCs [see  
205 panel (b) of Figure 5]. Focusing on the time evolution of southern cyclones' sizes, we note both a  
206 general decrease and a sort of pulsation in the distribution of the dimensions: namely, sometime the  
207 cyclones are quite different from each other, but at other times their sizes are more similar. Also,  
208 from the cloudiness point of view, the NPC differs from the surrounding cyclones showing an average  
209  $\tau$  of 3.4 while its CPCs have an average value of 2.1. The opposite happens for the SPC whose  
210 cloudiness ( $\tau \approx 2.2$ ) is systematically lower than the average cloudiness of the surrounding CPCs  
211 ( $\tau \approx 2.8$ ). The SPC cloudiness grows significantly reaching values similar to the NPC during the last  
212 part of the time period analyzed. Finally, in general, the cyclones are characterized by the tendency  
213 to reduce or maintain more or less their cloudiness when growing in size [see panel (d) of Figure 5].  
214 In a couple of cases we observed the opposite behavior.  
215

### 216 3. Spectral Analysis

217 To get more insights on the behavior of the CPC we have used the spectra recorded by JIRAM to  
218 obtain the atmospheric and cloud composition in relatively clear areas in the polar regions. The  
219 performed spectral analysis is limited to the wavelength range between 4 and 5  $\mu\text{m}$  and considers  
220 only the thermal emission of the planet. This enables to monitor in the same way the atmosphere both  
221 when illuminated and when not illuminated by the sun. In fact, in the brightest areas examined in our  
222 work the scattered solar contribution in the 4-5  $\mu\text{m}$  region is expected to be between 100 and 800  
223 times smaller than the thermal component, as previously reported by Drossart et al. [1998].

224 Most of the polar regions of Jupiter are affected by thick cloud coverage but relatively clear areas  
225 (with cloud total opacities  $< 1$  at 5  $\mu\text{m}$ ) exist at some specific locations, similar to the hot spots  
226 frequently observed between the Equatorial Zone and the North Equatorial Belt [Grassi et al. 2017a].  
227 Figure 6 shows the polar areas within  $80^\circ$  N/S latitudes where the optical depth,  $\tau$ , is lower than 1 at  
228 PJ4. Correspondingly, Figure 6 shows the areas where the JIRAM spectra are sensitive to the contents  
229 of ammonia, water vapor, phosphine and – in lesser degree – germane, at the approximate levels  
230 between 2 and 3 bar [Grassi et al. 2017b], well below Jupiter's tropopause level. Water and ammonia  
231 are condensable and involved in the cloud formation while germane and phosphine are disequilibrium

232 species from the deep interior and they are retrievable from JIRAM spectral data in the range 4.5-5.  
233  $\mu\text{m}$ .

234 The set of parameters to be retrieved has been defined following the scheme already proposed in  
235 Irwin et al. [1998] for hot spots. The adopted scheme aims to distinguish, where relevant, the 'deep'  
236 content of gaseous species from their mixing ratios in the upper troposphere, where depletion may  
237 occur due to condensation or photochemistry. According to that scheme, for the analysis here, we  
238 consider different free parameters:  $\text{H}_2\text{O}$ ,  $\text{NH}_3$ ,  $\text{PH}_3$ , and  $\text{GeH}_4$  "deep" mixing ratios, which are all  
239 assumed to be constant with altitude; the  $\text{H}_2\text{O}$  relative humidity above its condensation level and  
240 constant with altitude; and the total optical depth at  $5\mu\text{m}$  of the main (putative  $\text{NH}_4\text{SH}$ ) cloud above  
241 the water cloud. The topmost cloud layer (putatively  $\text{NH}_3$ ) is thought to be essentially absent in hot-  
242 spot regions, while diffuse haze has been demonstrated to be transparent at  $5\mu\text{m}$ .

243 Figure 7 displays the spectral region used for the retrieval. It also shows how the model used in the  
244 retrieval is able to reproduce the measured spectrum. Performance of the retrieval code has been  
245 quantified on the basis of test runs on large sets of simulated observations and the retrieval errors  
246 include the effects of forward-modelling errors in the radiative transfer. Notably, these errors exceed  
247 by at least a factor of 10 the instrumental Noise Equivalent Radiance, as estimated in Adriani et al.  
248 [2016]. Considering the typical nominal values of retrieval errors and assuming a mean deterioration  
249 factor 5 for all gases, we can estimate the approximate uncertainties for the retrieved contents of  
250 different gases from individual spectra as follows:  $\text{Log}_{10}([\text{H}_2\text{O}]_{\text{RH}}) \sim 0.08$ ,  $[\text{NH}_3] \sim 30$  ppm,  $[\text{PH}_3]$   
251  $\sim 60$  ppb and  $[\text{GeH}_4] \sim 0.043$  ppb. As water vapor is by far the most variable gas in the Jupiter  
252 atmosphere, it is more appropriate to express its abundance using the logarithm of relative humidity  
253 (i.e.: the original state vector element in our retrieval code) rather than use the mixing ratio.

254 Our retrieval model uses the temperature-vs-pressure profile from Seiff et al. [1998] on the basis of  
255 the Galileo Entry Probe measurements. In order to quantify errors introduced by possible variations  
256 of the real temperature with respect to the assumed value, numerical tests demonstrate that a  
257 systematic increase or decrease of 5K at every fixed pressure level of our atmospheric model induces  
258 a relative variation of about 2% in the retrieved contents of ammonia and phosphine, of 5% in  
259 germane and 15% in the water relative humidity value.

260 The analysis presented here was performed on PJ4 data (February 2<sup>nd</sup>, 2017). The method is described  
261 in more detail by Grassi et al. [2017b] and the analysis is restricted to spectra with low emission angle  
262 to limit retrieval uncertainties and attain higher signal.

263 Results of the analysis are reported in Figures 7 and 8 for the relative humidity of water vapor and  
264 the concentrations of ammonia, phosphine and germane, for the North and South Poles, respectively.  
265 The thickness of the tracks is proportional to the pixel resolution at Jupiter's 1-bar level. It is  
266 noticeable that the abundances of condensable species ( $\text{H}_2\text{O}$  and  $\text{NH}_3$ ) are more depleted over the  
267 lower-opacity regions. However, those gases appear relatively enhanced over the South Pole  
268 compared to northern regions, possibly because of smaller overall opacity of cyclones in the former  
269 areas during Juno PJ4 passage. Values range between 0.3% and 10% for the water vapor relative  
270 humidity and between 100 and 500 ppm for the ammonia mixing ratio in the north (see Figure 8),  
271 and between 0.3% and 20% for both for the water vapor relative humidity and ammonia in the south,  
272 but with an average significantly shifted toward the upper value (see Figure 9).

273 Areas with the lowest cloud cover are found to be considerably depleted in disequilibrium species

274 (PH<sub>3</sub> and GeH<sub>4</sub>) once compared against moderately cloudy ones, suggesting effective suppression of  
275 vertical upwelling (see Figures 7 and 8). PH<sub>3</sub> has abundances of the order of 0.6-1 ppm in the north  
276 while it reaches up to 2 ppm in the south. Also the GeH<sub>4</sub> shows the same difference between north  
277 and south with values of 6-10 ppb values that reach 15 ppb respectively. However, the comparison  
278 of absolute values between the two poles must also consider the better spatial resolution of the  
279 southern spectra for most of the JIRAM data, capable therefore of singling out more extreme values.

280 PH<sub>3</sub> and GeH<sub>4</sub> are not stable at the pressure and temperature conditions of the upper troposphere  
281 where they are detected. They are usually interpreted as tracers of active vertical motions that  
282 replenish the upper levels with fresh material from the much deeper atmosphere, where they are in  
283 equilibrium. The concentration contrasts between bright and dark area appear stronger over the  
284 northern pole and the depletion of germane looks stronger than for phosphine (see Figure 10). The  
285 ratio [PH<sub>3</sub>]/[GeH<sub>4</sub>] is of order a thousand.

286

#### 287 **4. Dynamics**

288 An analysis to understand the structure of the polar cyclones has been performed by attempting a  
289 comparative power spectrum investigation of long-living mesoscale (~100 km diameter) cyclones in  
290 Earth's ocean. In fact, the semi-stable, turbulent instabilities observed at Jupiter's Poles within and  
291 around the patterns of cyclones are reminiscent of the dynamics and instabilities observed in the  
292 buoyancy distributions in the Earth's oceanic mixed-layer [McWilliams, 2016] or in the potential  
293 temperature anomalies in the upper tropopause [Hakim et al. 2002]. In the ocean, these instabilities  
294 develop at scales smaller than the local Rossby deformation radius, between few hundred meters and  
295 2-3 km, and contribute to the internal structure of mesoscale vortices and to very large vertical  
296 velocities and intense vertical exchanges [e.g Zhong et al., 2017]. They are associated with the  
297 development of fronts at scales where the planetary rotation is still important but not dominant, and  
298 are characterized by intense vertical velocities [McWilliams, 2016].

299 The emergence of these kilometer-scale fronts cannot generally be described by quasigeostrophic  
300 (QG) models, developed by Charney [1971] to describe in a conceptually simple, two-dimensional  
301 framework, the dynamics of atmospheric and oceanographic flows with horizontal length scales  
302 which are very large compared to their vertical extension whenever the strength of inertia is small  
303 compared to the strength of the Coriolis force. On the other hand, the laterally divergent flows  
304 associated with frontogenesis are approximated in two-dimensions whenever the QG model is applied  
305 to a semi-infinite domain with zero potential vorticity (PV) in the interior. In this special case the so-  
306 called Surface Quasi-Geostrophy (SQG) approximation, first introduced by Blumen [1978] assumes  
307 that the flow evolution is controlled by the advection–diffusion of surface buoyancy at the boundary.  
308 It is based on the conservation of this active scalar (surface buoyancy) along the horizontal  
309 geostrophic flow, and links velocity and buoyancy.

310 The SQG model has shown some success in interpreting turbulent dynamics in the troposphere [Held  
311 et al. 1995], the dominance of cyclones over anticyclones at the tropopause [Hakim et al. 2002], and  
312 more recently, observations in the oceanic mixed-layer [Lapyere and Klein, 2006].

313 One characteristic that sets apart SQG, and flows in the oceanic mixed-layer, from “traditional” QG  
314 and two-dimensional turbulent flows is the slope of the energy power spectra, which is shallower  
315 than the non-local  $E(k) \propto k^{-3}$  predicted for two-dimensional and QG systems in the direct cascade

316 range [e.g. Bracco et al., 2004; Bracco and McWilliams, 2010]. An energy spectrum as steep or  
317 steeper than  $k^{-3}$  is indicative of non-local dynamics, where coherent, large scale vortices dominate.  
318 The theoretical SQG slope of buoyancy variance in the direct energy cascade range is indeed  $\propto k^{-5/3}$ ,  
319 indicative of local dynamics, where frontal and filamentary structures at scales smaller than the large  
320 coherent vortices control mixing. These local dynamics are behind the large vertical velocities and  
321 their localization in circulations of scales smaller than the Rossby deformation radius of the flow.  
322 Numerical simulations in various configurations using both the SQG approximation, or the primitive  
323 equations commonly employed by ocean models, concur in finding spectral slopes slightly steeper  
324 than  $k^{-5/3}$  and usually approaching  $k^{-2}$  [Pierrhumbert et al., 1994; Held et al., 1995; Capet et al., 2008;  
325 Zhong and Bracco, 2013]. The steepening of the theoretical slope is commonly found in presence of  
326 large vortices, but could also be related to numerical diffusion.

327 In Figure 11, the power spectra calculated on the full two-dimensional image mosaics return slopes  
328 consistent with the SQG model. The analysis done here follows the empirical correspondence  
329 between power spectra of atmospheric kinetic energy and those of cloud opacities as shown by  
330 Harrington et al. [1996] for Jupiter, on the basis of Travis [1978] previous results on Venus and Earth.  
331 Travis, in fact, found a close correspondence between power spectra of atmospheric kinetic energy  
332 and power spectra of visible and infrared cloud intensities. The same figure shows an eddy obtained  
333 integrating the SQG equation using a pseudo-spectral code and resolution  $1024 \times 1024$  grid points  
334 over a  $2\pi \times 2\pi$  non-dimensional domain; the eddy occupies nearly  $1/4$  of the model domain. The  
335 cyclone's energy spectra are shown with that of the whole domain including two more cyclonic  
336 eddies, and the spectrum of an upper ocean cyclone simulated by the Regional Ocean Modeling  
337 System [ROMS, Shchepetkin and McWilliams, 2005] at 750 m horizontal resolution [Gula et al.,  
338 2015].

339 The power spectra consistency is supported by a visual similarity, but other turbulent systems are  
340 characterized by analogous slopes. For example, recent work [Novi et al. 2019] has shown that rapidly  
341 rotating convective flows can generate intense vortices close to the poles on a spherical planet in local  
342 Cartesian approximation. These convective flows also have slopes close to  $k^{-2}$  but the structure of  
343 convective plumes and their vertical velocities appear to be more disorganized within the eddy [see,  
344 for a convective cyclonic plume in the high latitude Earth's ocean, Fig. 4 in Sun et al., 2017].

345

## 346 5. Conclusions

347 Jupiter's polar cyclonic structures on both northern and southern polar regions show no considerably  
348 changes during the two years of JIRAM observation considered in this study (February 2017 -  
349 February 2019). Differences between Jupiter's North Pole and South Pole are evident not only by  
350 counting the number of persistent cyclonic structures or the anticyclonic activity but also by other  
351 properties such as cloudiness, size, and concentration of minor and trace atmospheric species such as  
352 water vapor, ammonia, phosphine and germane. The question is whether these differences are only  
353 the consequence of an evolution of the two polar zones that proceeds on different time scales or,  
354 instead, there is a persistent and more profound connection with the deepest part of the Jovian  
355 atmosphere, such as its magnetic field which results to have a very different structures between north  
356 and south. In relation to the stability of the vortex configurations found at Jupiter's poles, Reinaud  
357 [2019] recently investigated the conditions under which an array of  $m$  three-dimensional, unit Burger  
358 number, quasi-geostrophic vortices on a ring, with an additional vortex lying on the array center, are



359 in mutual equilibrium. He found that the central vortex, if moderate in strength and having the same  
360 rotation sign of the peripheral ones, stabilizes the vortex array for a long time in a QG system. He  
361 refers specifically to the cluster of cyclones of Jupiter's polar regions as an example of environmental  
362 context where his study can be applied. On the other hand, our comparative analysis shows similar  
363 results for cyclones in both the Jupiter and the Earth's case cyclone in the upper ocean mixed-layer,  
364 with the size of the cyclones being proportional to the size of the planet to which they belong to. It  
365 also suggests the possibility of a well-mixed upper boundary layer on Jupiter's Poles with the  
366 cyclones being key mediators of any exchange with deeper layer(s) though large vertical velocities  
367 localized in frontal regions that result from local, non-geostrophic dynamics. Indications of the  
368 possible presence of fronts come from the strong gradients in optical depth and small scale structure  
369 in and around the cyclones. Finally, although our work on JIRAM data has provided insights into the  
370 dynamics of Jupiter's polar regions, additional measurements from Juno's other instruments, like the  
371 Juno's MicroWave Radiometer (MWR) which is able to sound deeper in the atmosphere, and  
372 corresponding analyses are necessary to explain the origin of Jupiter's curious polar cyclones.

373  
374

### 375 **Acknowledgements and Data Statement**

376 This work was supported by the Italian Space Agency through ASI-INAF contract I/010/10/0 and  
377 2014-050-R.0.

378 AA, DG, MLM, AMu, FA, AMi, RN, AC, RS, GS, CP, BMD, AT, GF, GP, and FT were supported  
379 by ASI. GO was supported by NASA with funds distributed to the Jet Propulsion Laboratory,  
380 California Institute of Technology. AI, SKA, JIL, and SJB were supported by the Juno Project. AB  
381 was supported by NSF OCE through grant 1658174.

382 The JIRAM instrument was developed by Leonardo at the Officine Galileo - Campi Bisenzio site.

383 JIRAM data is available on the Planetary Data System at:

384 [https://pds-atmospheres.nmsu.edu/data\\_and\\_services/atmospheres\\_data/JUNO/jiram](https://pds-atmospheres.nmsu.edu/data_and_services/atmospheres_data/JUNO/jiram) (Noschese and  
385 Adriani, 2017a, 2017 b).

386 Maps were done by using ENVI and the analysis for the dynamical chapter were done using Matlab.

387 The SQG spectral model can be found at the link:

388 <https://zenodo.org/badge/latestdoi/212413154>.

389 All the data used for preparing the figures can be found at the link:

390 <http://dx.doi.org/10.17632/mg2nskjzm2.1>.

391  
392

393

### 394 **References**

395

396 Acton, C.H. (1996). Ancillary data services of NASA's Navigation and Ancillary Information Facility  
397 *Planetary and Space Science*, 44, 65-70, doi: 10.1016/0032-0633(95)00107-7

398 Adriani, A., et al. (2016) Juno's Earth flyby: the Jovian infrared Auroral Mapper preliminary results.  
399 *Astrophysics and Space Science*, 361 (8), article id.272.

- 400 Adriani, A., Mura, A., Orton, G., Hansen, C., Altieri, F., Moriconi, M.L., Rogers, J., Eichstädt, G. et  
401 al. (2018). Clusters of Cyclones Encircling Jupiter's Poles. *Nature*, 555, 216-219, doi:  
402 [10.1038/nature25491](https://doi.org/10.1038/nature25491)
- 403 Adriani, A., Filacchione, G., Di Iorio, T., Turrini, D., Noschese, R., Cicchetti, A., Grassi, D., Mura,  
404 A., et al. (2017). JIRAM, the Jovian Infrared Auroral Mapper. *Space Science Reviews*, 213,  
405 393-446, doi: 10.1007/s11214-014-0094-y
- 406 Blumen, W. (1978). Uniform potential vorticity flow: Part I. Theory of wave interactions and two-  
407 dimensional turbulence. *Journal of Atmospheric Science*, 35, 774–783.
- 408 Bolton, S.J., Lunine, J.I., Stevenson, D., Connerney, J.E.P., Levin, S., Owen, T. C., Bagenal, F.,  
409 Gautier D., et al. (2018). The Juno Mission. *Space Science Reviews*, 213, 5-37, doi:  
410 10.1007/s11214-017-0429-6.
- 411 Bracco, A. & McWilliams, J.C. (2010). Reynolds-number dependency in homogeneous, stationary  
412 two-dimensional turbulence. *Journal of Fluid Mechanics*, 646, 517-526.
- 413 Bracco A., J von Hardenberg, A. Provenzale, J. Weiss & J.C. McWilliams (2004). Dispersion and  
414 mixing in quasigeostrophic turbulence, *Physical Review Letters*, 92, 084501-1 - 4
- 415 Capet X., Klein P., Hua B.L. Lapeyre, G., & McWilliams J.C., (2008), Surface kinetic and potential  
416 energy transfer in SQG dynamics. *Journal of Fluid Mechanics*, 604, 165–174.
- 417 Charney, J.G. (1971). Geostrophic turbulence. *Journal of Atmospheric Science*, 28, 1087–1095, doi:  
418 10.1175/1520-0469(1971)028<1087:GT>2.0.CO;2
- 419 Drossart, P., et al. (1998) The solar reflected component in Jupiter's 5- $\mu\text{m}$  spectra from NIMS/Galileo  
420 observations, *J. Geophys. Res.*, 103 (E10), doi:10.1029/98JE01899
- 421 Giles, R.S., Fletcher, L.N., & Irwin P.G.J. (2015). Cloud structure and composition of Jupiter's  
422 troposphere from 5-m Cassini VIMS spectroscopy, *Icarus*, 257, 457-470,  
423 doi:10.1016/j.icarus.2015.05.030.
- 424 Giles, R.S., Fletcher, L.N., & Irwin P.G.J. (2017). Latitudinal variability in Jupiter's tropospheric  
425 disequilibrium species: GeH<sub>4</sub>, AsH<sub>3</sub> and PH<sub>3</sub>, *Icarus*, 289, 254-269,  
426 doi:10.1016/j.icarus.2016.10.023.
- 427 Grassi, D., Adriani, A., Mura, A., Dinelli, B.M., Sindoni G., Turrini D., Filacchione, G., Migliorini,  
428 A., et al (2017a). Preliminary results on the composition of Jupiter's troposphere in hot spot  
429 regions from the JIRAM/Juno instrument. *Geophysical Research Letters*, 44 (10), 4615-4624,  
430 doi:10.1002/2017GL072841.
- 431 Grassi, D., Ignatiev, N.I., Sindoni, G., D'Aversa E., Maestri T., Adriani, A., Mura, A., Filacchione,  
432 G., et al (2017b). Analysis of IR-bright regions of Jupiter in JIRAM-Juno data: Methods and  
433 validation of algorithms. *Journal of Quantitative Spectroscopy and Radiative Transfer*, 202,  
434 200-209, doi:10.1016/j.jqsrt.2017.08.008.
- 435 Gula, J., Molemaker M.J. & McWilliams, J.C. (2015). Gulf Stream dynamics along the southeastern  
436 U.S. Seaboard. *Journal of Physical Oceanography*, 45, 690–715, doi:10.1175/JPO-D-14-  
437 0154.1.

- 438 Irwin, P.G.J., Weir, A.L., Smith, S.E., Taylor, F.W., Lambert, A.L., Calcutt, S.B., Cameron-  
439 P.J., Carlson R.W., et al. (1998). Cloud structure and atmospheric composition of Jupiter  
440 retrieved from Galileo near infrared mapping spectrometer real-time spectra. *Journal of*  
441 *Geophysal Research Planets*, 103 (E10), 23001-23021, doi:10.1029/98JE00948.
- 442 Hakim G.J., Snyder C. and Muraki D. J. (2002), A new surface model for cyclone–anticyclone  
443 asymmetry. *J. Atmos. Sci.*, 59, 2405–2420.
- 444 Hansen, C.J. et al. (2014). Junocam: Juno’s Outreach Camera, *Space Sci. Rev.* doi 10.1007/s11214-  
445 014-0079-x.
- 446 Harrington J., T.E. Dowling, and R.L. Baron (1996). Jupiter Tropospheric Thermal Emission: II.  
447 Power Spectrum Analysis and Wave Search. *Icarus*, 124, 32-44, doi: 10.1006/icar.1996.0188
- 448 Held I.M., Pierrehumbert R.T., Garner S.T., et al (1995), Surface quasi-geostrophic dynamics. *J.*  
449 *Fluid Mech.* 282, 1–20.
- 450 Lapeyre G. and Klein P. (2006), Dynamics of the upper oceanic layers in terms of surface  
451 quasigeostrophy theory. *J. Phys. Oceanogr.*, 36, 165–176.
- 452 McWilliams JC. (2016), Submesoscale currents in the ocean. *Proc. R. Soc. A* 472: 20160117,  
453 <http://dx.doi.org/10.1098/rspa.2016.0117>
- 454 Noschese, R. and A. Adriani, JNO-J-JIRAM-2-RDR-V1.0, NASA Planetary Data System, 2017a.
- 455 Noschese, R. and A. Adriani, JNO-J-JIRAM-3-EDR-V1.0, NASA Planetary Data System, 2017b.
- 456 Pierrehumbert, R.T., I.M. Held and K.L. Swanson (1994) Spectra of local and nonlocal two-  
457 dimensional turbulence. *Chaos, Solitons, Fractals* 4, 1111–1116.
- 458 Reinaud J.N. (2019), Three-dimensional quasi-geostrophic vortex equilibria with m-fold symmetry,  
459 *J. Fluid Mech.*, 863, 32\_59, Cambridge University Press 2019, doi:10.1017/jfm.2018.989
- 460 Seiff, A. et al. (1998) Thermal structure of Jupiter's atmosphere near the edge of a 5- $\mu$ m hot spot in  
461 the north equatorial belt, *J. Geophys. Res.*, 103 (E10), doi:10.1029/98JE01766. Available as  
462 numerical data as GP-J-ASI-3-ENTRY-V1.0, NASA Planetary Data System.
- 463 Shchepetkin A.F., and J.C McWilliams JC. (2005), The regional oceanic modeling system: a split-  
464 explicit, free-surface, topography-following coordinate oceanic model. *Ocean Model* 9, 347–  
465 404. doi: 10.1016/j.ocemod.2004.08.002
- 466 Sun, D., T. Ito, & A. Bracco (2017) Oceanic uptake of oxygen during deep convection events through  
467 diffusive and bubble mediated gas exchange *Global Biogeochem. Cycles*, 31,  
468 <https://doi.org/10.1002/2017GB005716>
- 469 Travis L.D. (1978). Nature of atmospheric dynamics on Venus from power spectrum analysis of  
470 Mariner 10 images. *J. Atmos. Sci.*, 35, 1584-1595, doi: 10.1175/1520-  
471 0469(1978)035<1584:NOTADO>2.0.CO;2
- 472 Zhong, Y., A. Bracco, J. Tian, J. Dong, W., Zhao, Z. Zhang (2017), Observed and simulated vertical  
473 pump of an anticyclonic eddy in the South China Sea. *Scientific Report* , 44011,  
474 doi:10.1038/srep44011
- 475 Zhong Y., and A. Bracco (2013), Submesoscale impacts on horizontal and vertical transport in the  
476 Gulf of Mexico, *J. Geoph. Res. - Oceans*, 118, 5651-5668, doi:10.1002/jgrc.20402

477

478

479

Author Manuscript

Date	Orbit #	Orbit type	Pole	Average Resolution	Images #
02/02/2017	4	MWR	North	51 km	9
			South	55 km	11
05/19/2017	6	MWR	North	23 km	45
			South	59 km	12
09/01/2017	8	GRAV	South	47 km	18
10/24/2017	9	MWR	North	39 km	40
			South	16 km	40
12/16/2017	10	GRAV	North	15 km	14
02/07/2018	11	GRAV	South	44 km	17
05/24/2018	13	GRAV	South	53 km	12
07/16/2018	14	GRAV	South	57 km	10
09/07/2018	15	GRAV	South	61 km	23
12/21/2018	17	GRAV	South	49 km	16
02/12/2019	18	GRAV	South	46 km	14

481

482

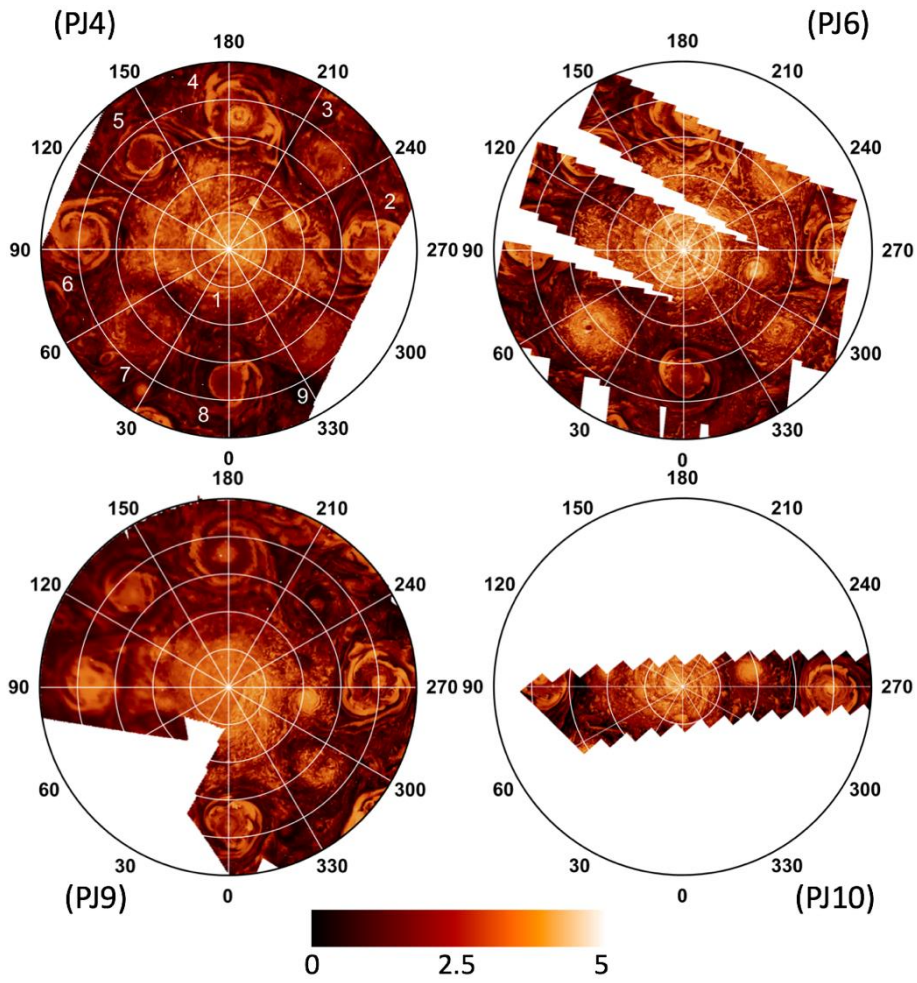
483

484

485

486

**Table 1.** Summary of the polar observations. The average resolution reported here is calculated at 1-bar level and it is referred to the mosaics shown in Figures 1, 2 and 3. It is the result of the resampling of the single images at a homogeneous spacing. Last column shows the number of images used for composing the mosaics of Figures 1,2 and 3.



487

488

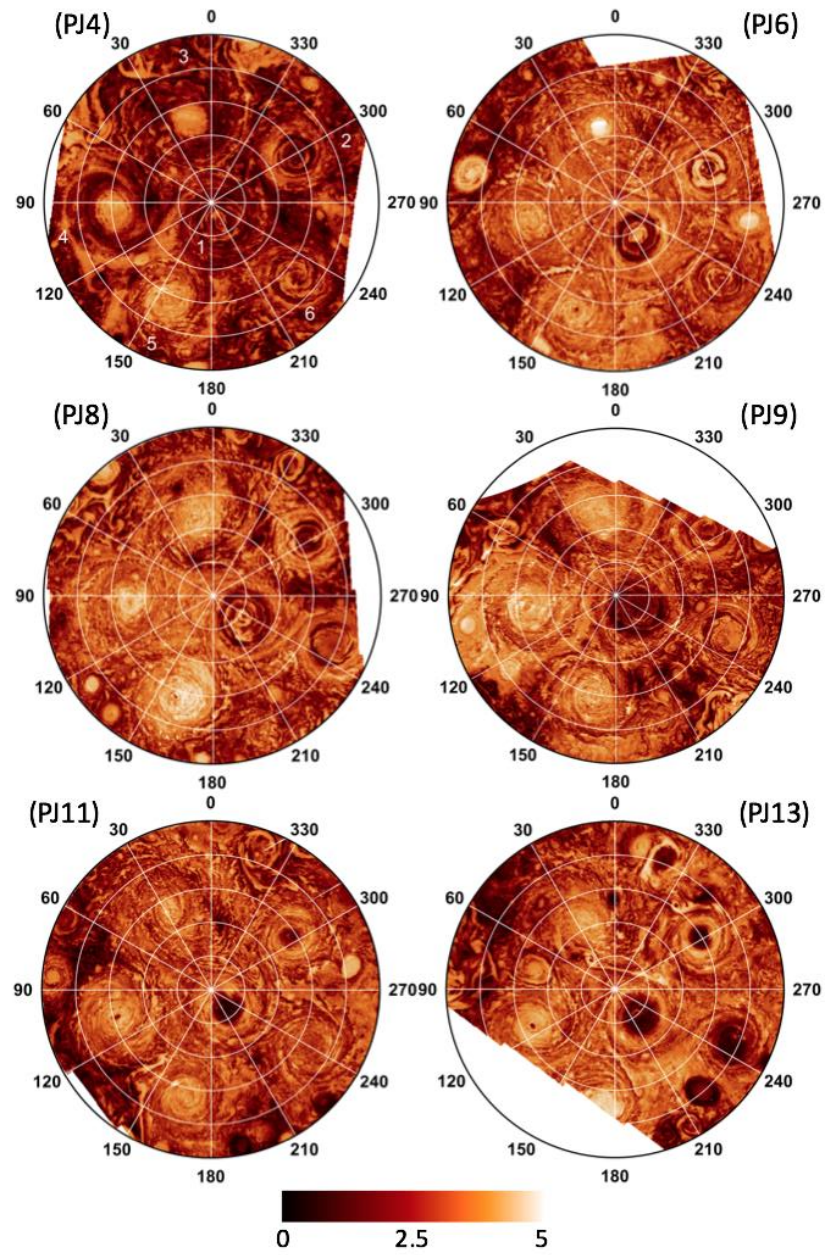
489

490

491

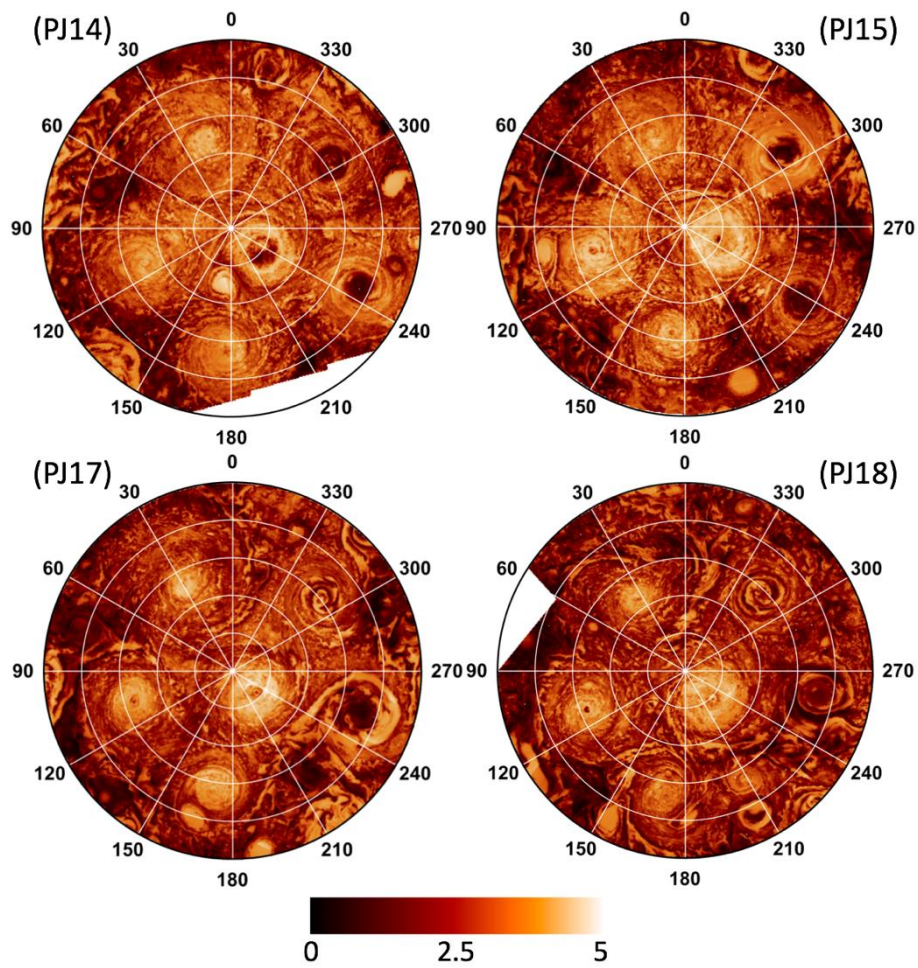
492

**Figure 1.** North pole during PJ4, PJ6, PJ9 and PJ10 (from top to bottom al left from right). Whitish colors indicate higher optical depth ( $\tau$ ), i.e. thicker clouds. Cyclone numbering: the polar cyclone is #1; the cyclone at 90E is #2; the numbering proceeds counterclockwise from #3 to #9. The color bar on the bottom indicates the value of  $\tau$ .



494

495 **Figure 2.** South pole from PJ4 to PJ13 (from top to bottom al left from right). Whitish colors  
 496 indicate higher optical depth ( $\tau$ ), i.e. thicker clouds. Cyclone numbering: the polar cyclone is #1;  
 497 the cyclone at the longitude of approximately 120E is #2; the numbering proceeds counterclockwise  
 498 from #3 to #6. The color bar on the bottom indicates the value of  $\tau$ .  
 499

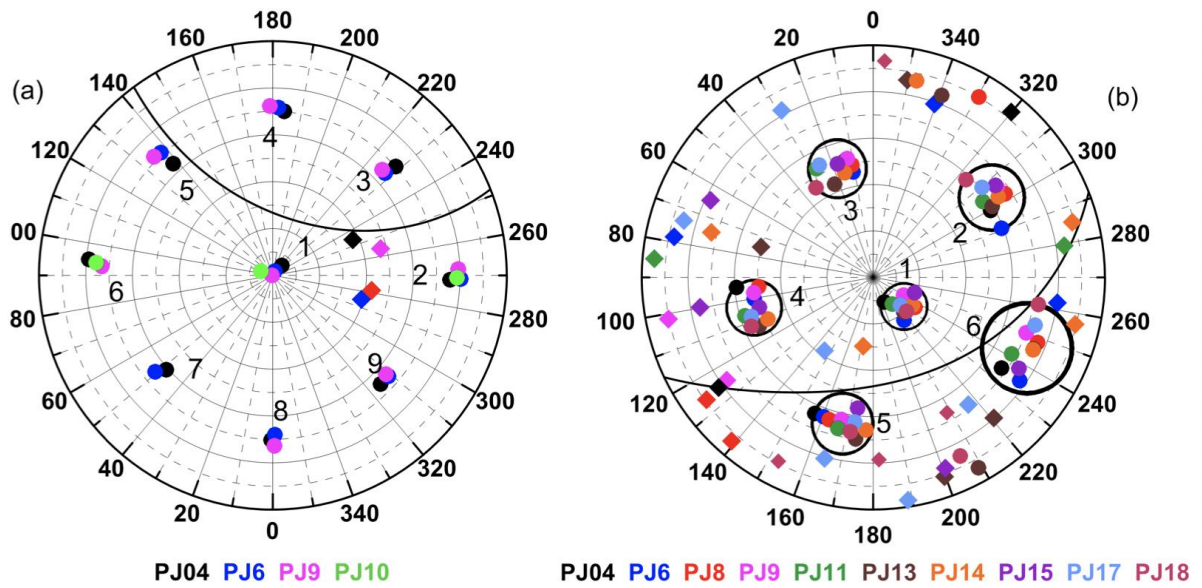


501

502 **Figure 3.** South pole during PJ14 to PJ18 (from top to bottom al left from right). Whitish colors  
 503 indicate higher optical depth ( $\tau$ ), i.e. thicker clouds. Cyclone numbering: the polar cyclone is #1; the  
 504 cyclone at the longitude of approximately 120E is #2; the numbering proceeds counterclockwise from  
 505 #3 to #6. The color bar on the bottom indicates the value of  $\tau$ .

506

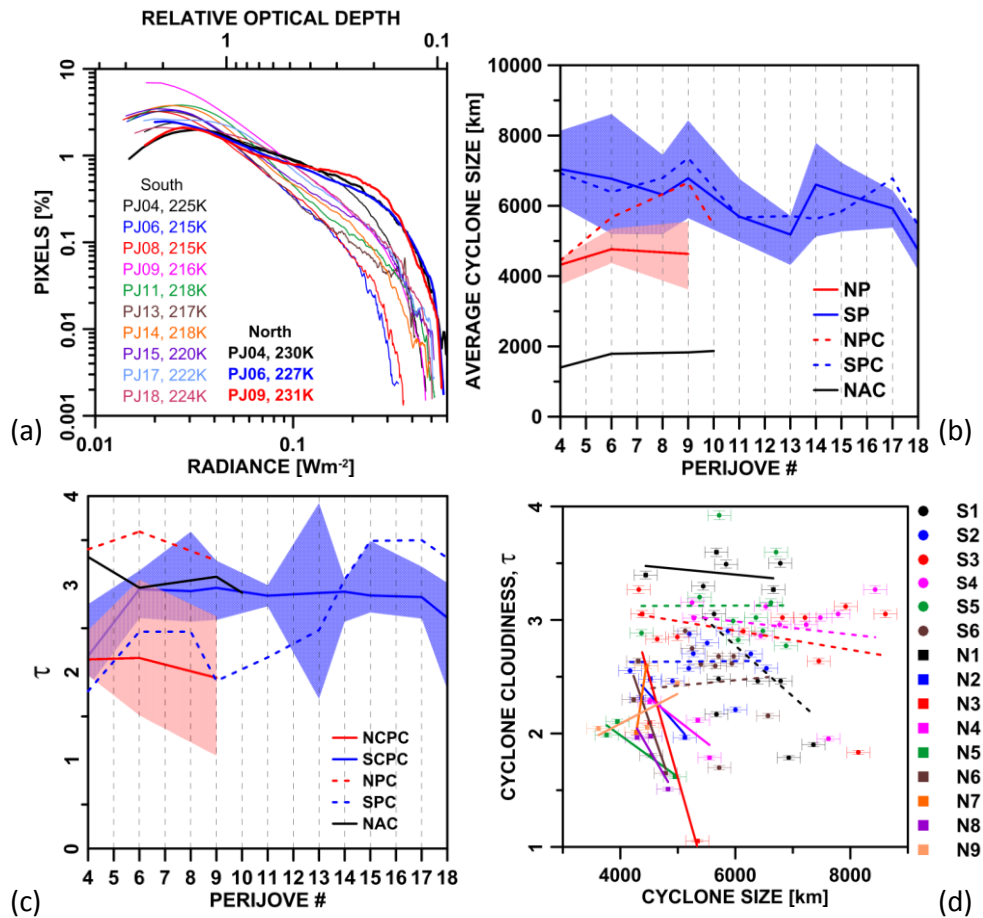




508

509 **Figure 4.** Position of the cyclone centers (dots) during the observation period for North pole [panel  
 510 (a)] and South pole [panel (b)]. The colors identify the different perijoves. The black circles indicate  
 511 the variation of the position of the southern cyclone centers and are centered at the average position  
 512 measured in the all period of observations. The diamonds represent the position of the different  
 513 anticyclones with diameters larger than 1000 km. The oval in panel (a) identify the different positions  
 514 of the same anticyclone during the different reported perijoves.

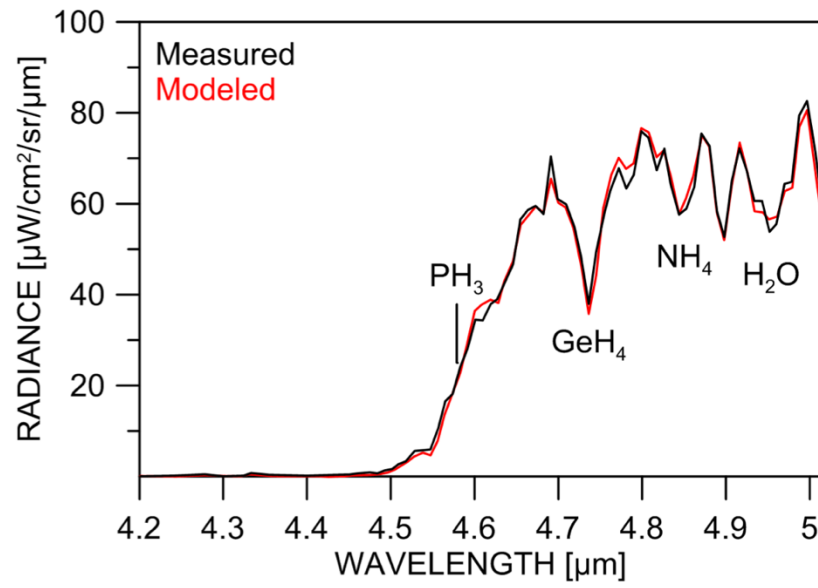
515



517

518 **Figure 5.** (a): Distribution of pixels radiance, the average brightness temperature at latitudes higher  
 519 than  $80^\circ$  is given for each perijove. (b): The blue and the red curves gives the average diameter of the  
 520 circumpolar cyclones for the south and the north respectively; the dashed curve account for the  
 521 respective polar cyclones; the blue and the red areas show the minimum to maximum variation of the  
 522 cyclones size; the black curve gives the diameter of the only larger anticyclone observed in the north;  
 523 (c): optical depth of cyclones, following the color definitions for panel (b). (d): optical depth versus  
 524 cyclone size; in the legend S stands for south and N for north and the numbering criterion is the same  
 525 given in figures 1, 2 and 3.

526

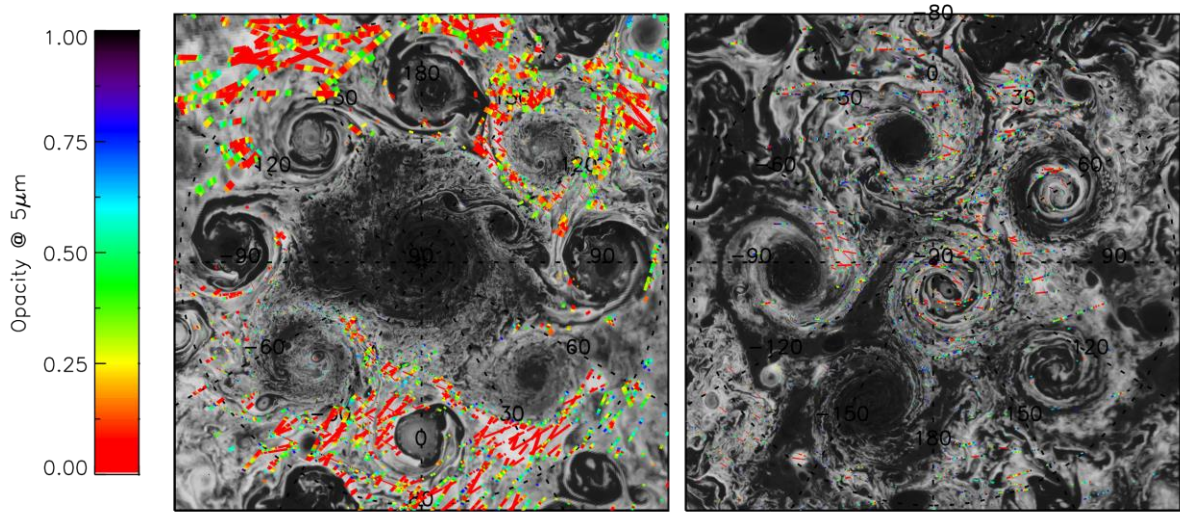


528

529

**Figure 6.** Comparison between a measured and a reconstructed spectrum between 4.2 and 5  $\mu\text{m}$ .

530



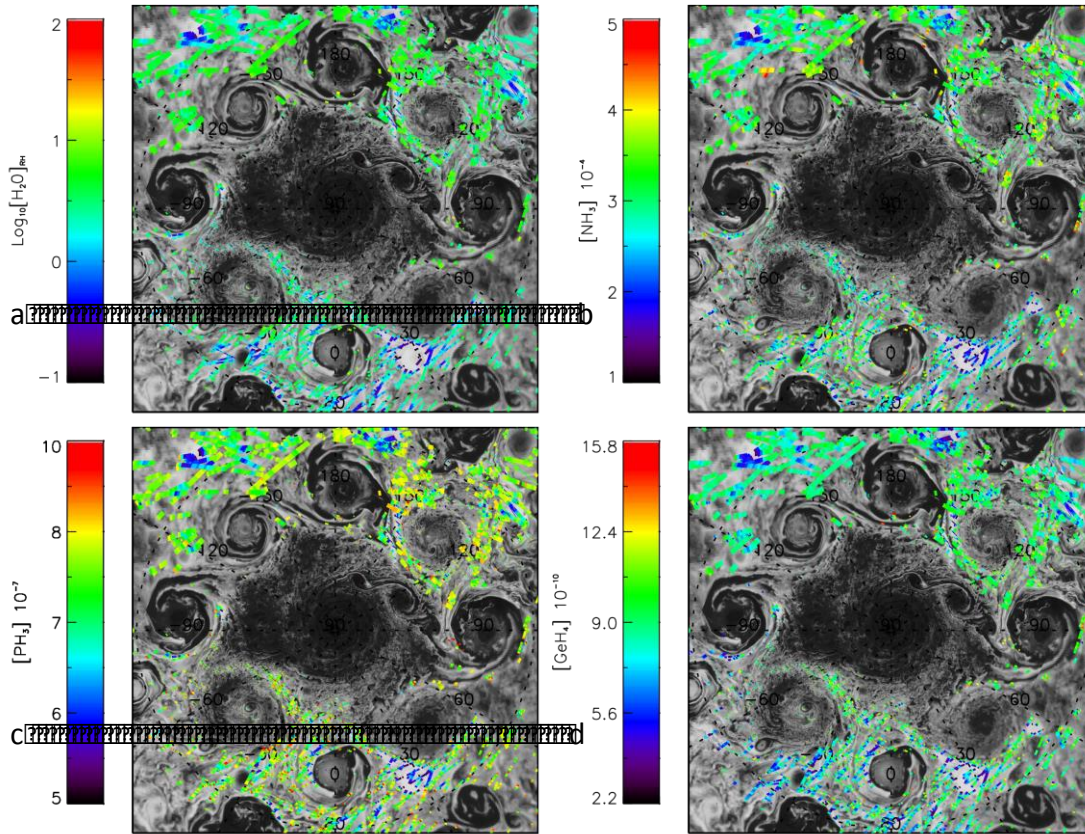
532

533

534

535

**Figure 7.** Areas where the optical depth, in the infrared wavelengths around  $5\ \mu\text{m}$ , is lower than 1 according to the JIRAM spectrometer data.



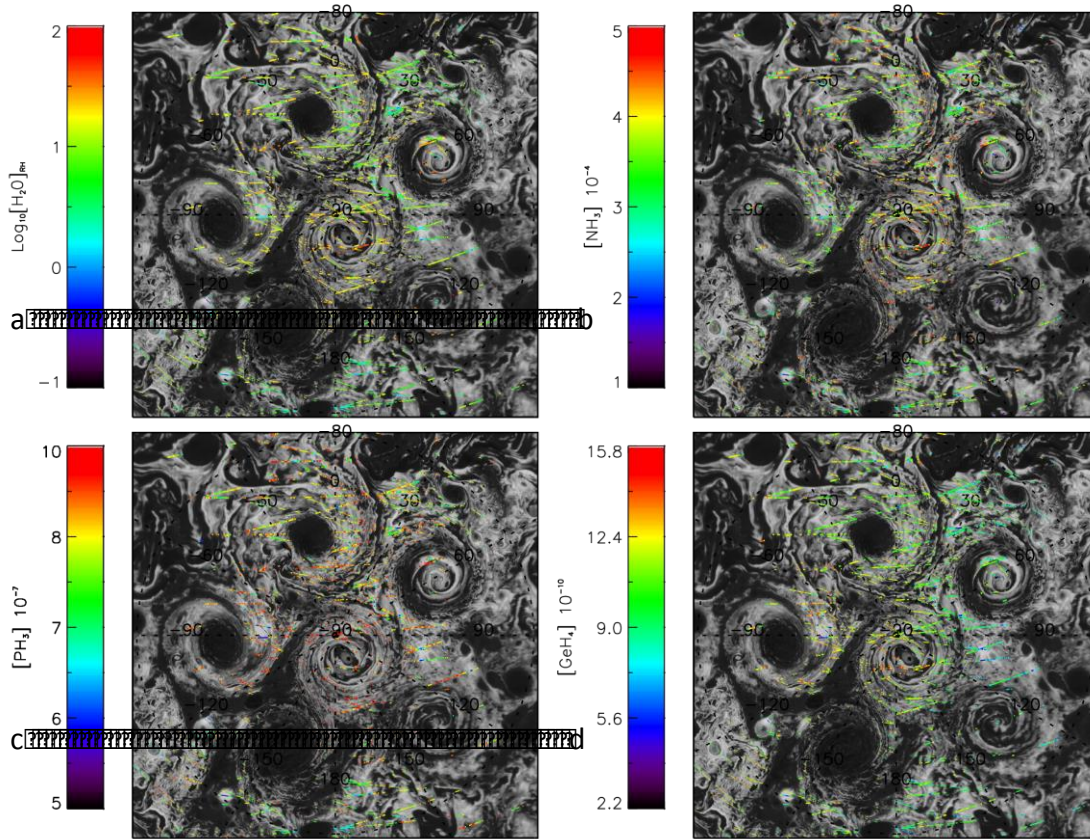
537

538

539

540

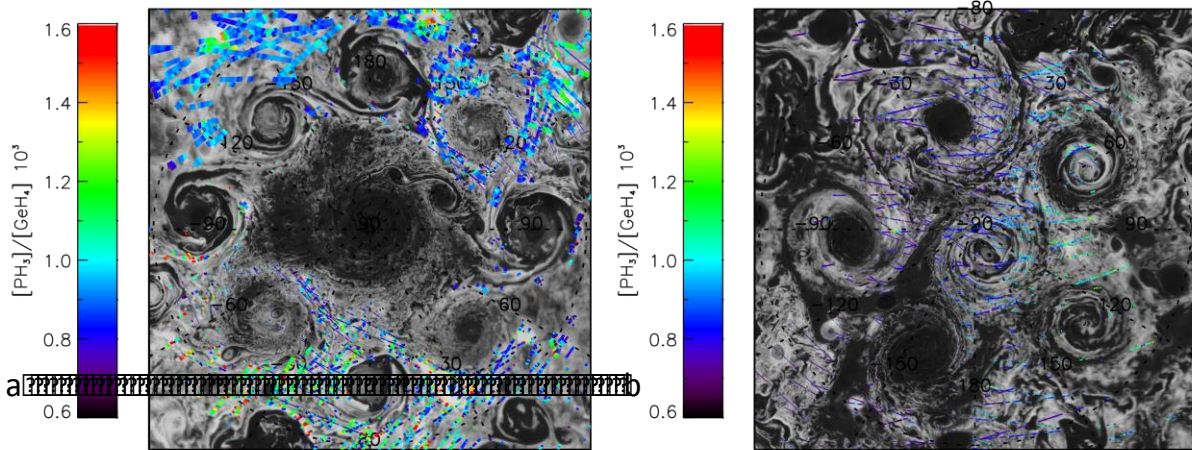
**Figure 8.** North pole maps of water relative humidity (a), ammonia (b), phosphine (c) and germane (d) concentrations.



542

543 **Figure 9.** South pole maps of water relative humidity (a), ammonia (b), phosphine (c) and germane  
 544 (d) concentrations.

545



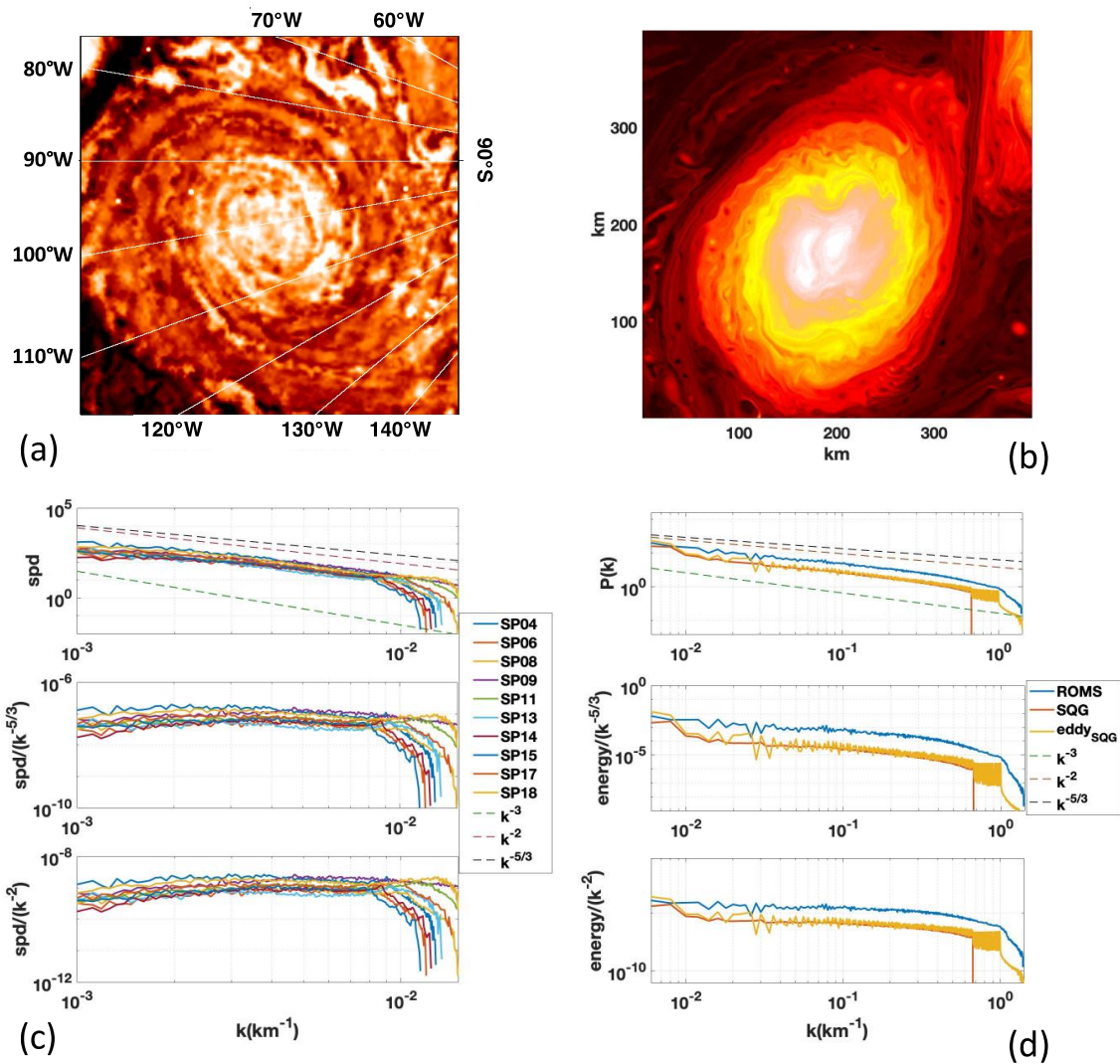
547

548

549

550

**Figure 10.** Maps of phosphine to germane ratio for the North (left panel) and for the South (right panel).



552

553

554

555

556

557

558

559

560

561

562

**Figure 11.** (a) Jupiter cyclone #4 from South Pole PJ4 image. (b) Cyclonic eddy in surface buoyancy in a freely-decaying SQG simulation at a resolution of 1024 x 1024. Several Gaussian shaped cyclones are seeded as initial conditions in a freely-decaying, unforced run. The figure shows one of the remaining cyclones after approximately 50 rotation periods. (c) 2D power spectra for selected data sets from Jupiter South Poles; the power spectra calculated for Jupiter are related to the latitudes higher than 82°S that are dominated by the presence of the polar cyclones. (d) 2D power spectra for the cyclone in panel (b) in light orange, for the whole SQG field at the time the cyclone was extracted in dark orange, and for an ocean cyclonic eddy obtained by ROMS run in the Gulf Stream region at horizontal resolution of 750 m [courtesy of J. Gula]. The ocean cyclone is approximately 200 km in diameter and the non-dimensional SQG eddy has been scaled to match it.